

AI-Based Pipeline for Automatic Quantification of Tissue Ingrowth in Histopathology Images of Cerebral Aneurysm

Ishaq Ansari^{a, b}, Ahmed Naglah^a, Lillian G. Atchison^a, Melanie E. Martinez^c,
Elizabeth Klaas^c, Koji Hosaka^c, Brian Hoh^c, and Pinaki Sarder^{a, †}

^aDivision of Nephrology, Hypertension & Renal Transplantation, College of Medicine,
University of Florida, Gainesville, FL, 32611

^bSchool of Natural Sciences, Caldwell University, Caldwell, NJ, 07006

^cDepartment of Neurosurgery, College of Medicine, University of Florida, Gainesville, FL,
32611

ABSTRACT

Cerebral aneurysm (CA) is a life-threatening condition caused by a weakened spot in the blood vessels of the brain that balloons out and fills with blood. The rupture of an aneurysm can lead to severe complications such as hemorrhagic stroke, brain damage, coma, and even death. Effective aneurysm therapy includes inducing intra-aneurysmal wound healing by promoting tissue ingrowth that seals off the aneurysm, thereby preventing rupture. Therefore, quantifying the extent of tissue ingrowth in the aneurysmal sac is crucial to understanding the progression of treatment and predicting the risk of rupture. In this study, we propose an AI-based pipeline to automatically segment and quantify ingrown tissue using a UNET-style deep learning model. We identify the boundary of the aneurysmal sac using the model and then apply subsequent processing steps to calculate the percentage of ingrown tissue. Our model achieved a high accuracy of 0.96 ± 0.01 in identifying and predicting the boundaries of the aneurysmal sacs based on our experiments with 64 images. Future work will focus on further refining the model for improved performance and exploring its application to predict the risk of aneurysm rupture based on tissue ingrowth patterns. By integrating our pipeline with clinical data, we aim to provide valuable insight into the progression of aneurysm treatment and improve patient safety.

Keywords: AI, UNET, deep learning pipeline, cerebral aneurysm, digital pathology, whole slide image analysis

1. INTRODUCTION

A cerebral aneurysm (CA), or brain aneurysm, is characterized by dilation at a weak or thin spot in the blood vessels of the brain, forming a sac that can burst under pressure of blood flow. It occurs in up to 5% of the general population¹ and, when ruptured, leads to serious health problems such as hemorrhagic stroke, brain damage, coma, and even death.² Subarachnoid hemorrhage (SAH), resulting from aneurysm rupture in which blood bleeds into the space between the brain and its covering membrane, is associated with 50% mortality and 30% dependency.³ An estimated 6.8 million people in the United States have an unruptured brain aneurysm, which is about one in 50 individuals.⁴ Aneurysms that are detected before they rupture can be treated. Therefore, preventing aneurysm rupture is crucial as it can significantly reduce mortality, dependency, and economic burden, improving patient outcomes and quality of life.

Current treatments for aneurysms include surgical clipping and endovascular coiling procedures to close off an aneurysm. In surgical clipping, the neurosurgeon removes a section of the skull to locate the blood vessel that feeds the aneurysm and places a tiny metal clip on the neck of the aneurysm to stop blood flow into it.⁵ With endovascular coiling, the surgeon feeds a soft flexible wire into the aneurysm via a catheter and coils it inside the aneurysm, sealing off the aneurysm.⁵ Coiling is safer than surgery,⁵ but the disadvantage of coiling is the significant rate of aneurysm recurrence and need for retreatment, which may occur in up to one-quarter of aneurysms.⁶ Surgically harvested and autopsy-derived specimens of human brain aneurysms demonstrate that

Send correspondence to: Pinaki Sarder, PhD; Email - pinaki.sarder@medicine.ufl.edu

durable aneurysm cure is achieved by intra-aneurysmal wound healing.⁷ These successful healings comprised connective tissue proliferation, fibroblasts, collagen, smooth muscle cells, capillary ingrowth, and macrophages.⁸ In response, we aim to understand the biology of the healing process by experimenting with different mediators to induce tissue ingrowth to achieve similar healing. The success of the treatment will be a significant milestone in the treatment of aneurysms, a treatment with better efficacy to prevent rupture while potentially reducing the rates of recurrence and retreatment.

Our aim is to quantify the amount of tissue ingrowth to monitor the progress of their treatment. Given the impracticality of manually analyzing the extensive data by a human pathologist, we thought of combining digital pathology with advanced machine learning to automate the analysis process, significantly reducing the time and effort required. However, despite the extreme success of deep learning technology in the field of computer vision, there are no existing pipelines designed to automatically segment and quantify ingrown tissue from whole slide images (WSI) of cerebral aneurysms. While the major applications in digital pathology using machine learning include automatic cancer classification, survival analysis, and subtyping from pathological images,⁹ research on cerebral aneurysms remains extremely limited. Therefore, our work addresses this critical gap by developing a specialized pipeline that can automatically identify and quantify the percentage of tissue ingrowth from hematoxylin and eosin (H&E) stained histopathology images of cerebral

2. MATERIALS AND METHODS

2.1 Dataset

The dataset consists of whole slide images of aneurysmal sacs obtained from the Department of Neurosurgery at University of Florida, College of Medicine. It comprised of 64 brightfield H&E stained whole slide images, each paired with corresponding annotations. We randomly splitted the dataset into training, validation, and test sets, with 40 used for training, 12 for validation, and 12 for testing. Given the small number of images, we utilized data augmentation techniques to artificially expand the training dataset. The 40 training datasets were augmented using HorizontalFlip, CoarseDropout, ScaledRotation, and RandomContrast, making a total of 200 images for training.

2.2 Segmentation model

To semantically segment the boundary of the aneurysmal sac from histopathology images, we adapted a UNET deep learning model tailored to this specific task. Unlike most pathological image analyses that are based on patch-wise processing, our model perform segmentation on whole slide images. Our proposed model is composed of 69 layers, including 18 convolutional layers, each followed by batch normalization and ReLU activation functions, enhancing feature extraction at multiple levels of abstraction. The architecture integrates 4 max pooling layers for downsampling, preserving essential features while reducing spatial dimensions. The decoding path utilizes 4 Conv2DTranspose layers and 2 ZeroPadding2D layers for upsampling, complemented by 4 concatenate layers to fuse multi-scale features. This deep hierarchical structure enables the model to capture complex patterns, making it highly effective for image segmentation.

In our model, we utilized several key components to enhance its performance. Adam algorithm was used to efficiently updates the network weights based on the loss gradient calculated using the Binary Cross-Entropy (BCE) loss function. Additionally, we incorporated the sigmoid activation function to ensure that the output values are mapped within the range of 0 to 1, which is crucial for probabilistic predictions. These components together contributed to a well-rounded training process and improved the model's effectiveness.

To monitor and control the training process, we implemented a series of callbacks. The model was saved at each epoch only if it achieved the best performance on the validation set, thereby preventing overfitting and conserving storage. Additionally, the learning rate was reduced by a factor of 0.1 if no improvement in validation loss was observed for four consecutive epochs. Training was halted after 20 consecutive epochs without improvement in validation loss, further mitigating overfitting risks.

Following the successful prediction of the complete sac boundary, we created a binary mask from the original image to delineate all tissue regions in white. This mask was then used in a scalar product operation with the sac zone masks to isolate the binary mask of the ingrown tissue regions. To quantify the ingrown tissue, we

calculated the ratio of white pixels in this ingrown-tissue mask relative to the total area of the sac zone, which represents the percentage of ingrown tissue within the sac boundary.

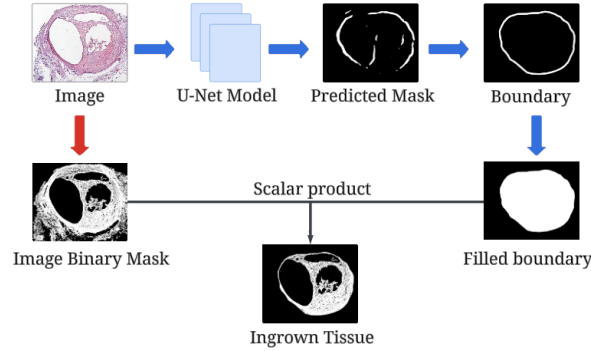


Figure 1. A graphical representation of the structure and workflow of the proposed pipeline for sac boundary prediction and quantification of ingrown tissue within the sac zone

3. RESULTS

Since accurately identifying the sac boundary is the first critical step in quantifying ingrown tissue, our initial focus was on training models using the sac boundary as the primary ground truth. This approach allowed us to calculate tissue ingrowth percentage from the predicted boundaries. Although our model successfully predicted the boundaries of the aneurysmal sacs, the manual thresholding of 0.5 resulted in incomplete boundaries. To address this, we explored various thresholding methods to identify the optimal threshold. We experimented with manual 0.5 thresholding, Li's thresholding method (eq. 1), and analyzed the Receiver Operating Characteristic (ROC) curve to determine the most effective thresholds. We applied the Youden Index (eq. 2) to maximize the difference between the True Positive Rate (TPR) and False Positive Rate (FPR), and the Distance to (0,1) (eq 3) to minimize the distance to the top-left corner of the ROC space, thus locating the optimal threshold.

$$\begin{aligned}\mu_1(T_k) &= \frac{1}{N_1} \sum_{x_i < T_k} x_i, \\ \mu_2(T_k) &= \frac{1}{N_2} \sum_{x_i \geq T_k} x_i, \\ T_{k+1} &= T_k - \frac{\mu_1(T_k) - \mu_2(T_k)}{\log(\mu_1(T_k)) - \log(\mu_2(T_k))}\end{aligned}\tag{1}$$

where, $\mu_1(T_k)$ is the mean of pixel intensities below the threshold, $\mu_2(T_k)$ is the mean of the pixel values above the threshold T_k , and T_{k+1} is the updated threshold based on the means.

$$\text{Youden Index} = \text{TPR} - \text{FPR}\tag{2}$$

$$\text{Distance to } (0, 1) = \sqrt{(1 - \text{TPR})^2 + \text{FPR}^2}\tag{3}$$

In addition to using the sac boundary, we tested models with the sac zone and ingrown tissue as alternative ground truths. The rationale for using the sac zone was that accurate identification of the sac zone would obviate the need for boundary completion, with the boundary becoming a contour of the prediction. Training with the ingrown tissue mask aimed to eliminate the scalar product step altogether, thereby streamlining the process and enhancing the model's robustness and reliability. The results of these experiments, including comparisons of thresholding methods, are presented in Figure 2.

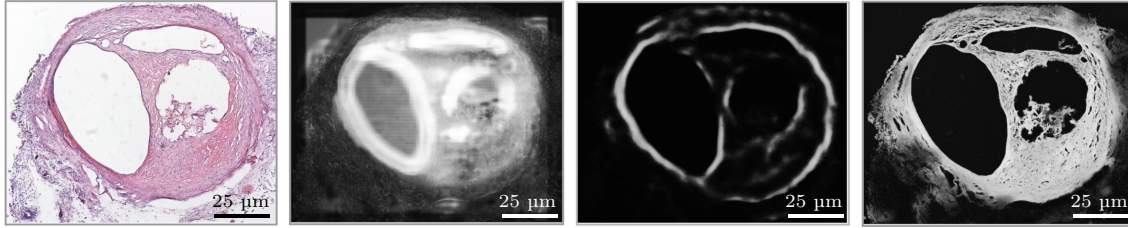


Figure 2. Predictions from the proposed pipeline for three different binary masks used. Starting from left: original image, predicted sac, predicted boundary, and predicted in-grown tissue.

The raw predictions above were post-processed using various thresholding, such as li, youden, distance from (0,0), and 0.5 thresholdings. The results, as per presented in Table 1, demonstrated that 0.5 thresholding method provided the highest accuracy and precision but struggled with incomplete boundary predictions, as indicated by the lower Jaccard index and recall. Li's thresholding method, while achieving the highest F1 score and recall, indicated better capture of true positives but at the cost of increased false positives. The Youden and Distance to (0,1) thresholds offered the best boundary overlap (highest Jaccard index) but show lower precision, reflecting a trade-off between capturing more true positives and minimizing false positives.

Table 1. Performance comparison of thresholding methods in post-processing of boundary predictions. The table shows the average results across 12 test images.

Masks	Thresholding Method	Accuracy	F1 Score	Jaccard	Recall	Precision
Sac Zone	0.5 Threshold	0.81 ± 0.06	0.57 ± 0.21	0.42 ± 0.20	0.60 ± 0.30	0.73 ± 0.22
	Li Threshold	0.77 ± 0.09	0.60 ± 0.21	0.46 ± 0.21	0.77 ± 0.25	0.52 ± 0.22
	Youden Threshold	0.78 ± 0.12	0.57 ± 0.18	0.87 ± 0.10	0.68 ± 0.14	0.53 ± 0.17
	Distance Threshold	0.80 ± 0.10	0.58 ± 0.18	0.81 ± 0.11	0.67 ± 0.16	0.52 ± 0.18
Boundary	0.5 Threshold	0.96 ± 0.01	0.30 ± 0.20	0.19 ± 0.15	0.27 ± 0.22	0.49 ± 0.16
	Li Threshold	0.89 ± 0.06	0.35 ± 0.09	0.22 ± 0.07	0.72 ± 0.22	0.25 ± 0.08
	Youden Threshold	0.84 ± 0.06	0.18 ± 0.05	0.88 ± 0.12	0.29 ± 0.08	0.17 ± 0.05
	Distance Threshold	0.85 ± 0.04	0.18 ± 0.05	0.86 ± 0.10	0.30 ± 0.08	0.18 ± 0.05
Tissue	0.5 Threshold	0.85 ± 0.07	0.37 ± 0.29	0.26 ± 0.23	0.45 ± 0.35	0.44 ± 0.32
	Li Threshold	0.82 ± 0.07	0.42 ± 0.27	0.30 ± 0.23	0.58 ± 0.35	0.38 ± 0.27
	Youden Threshold	0.72 ± 0.23	0.35 ± 0.24	0.80 ± 0.22	0.44 ± 0.27	0.32 ± 0.24
	Distance Threshold	0.76 ± 0.15	0.35 ± 0.26	0.74 ± 0.22	0.44 ± 0.28	0.32 ± 0.24

The choice of thresholding depends on the requirements of the project. For our project, we want the white pixels in the predicted mask to be the same white pixels that make the boundary (which is given by higher Jaccard values). However, since a high Jaccard score can sometimes be accompanied by noise, precision must also be considered. Therefore, the best threshold is one that achieves both high Jaccard and high precision values.

4. CONCLUSION

Our model's predictions for the all three masks achieve high accuracy, however, struggled for jaccard and precision. We expect to fine-tuning the model to balance precision and recall based on our project requirements and train the model on larger dataset.

It is also important to note that these results were obtained using only 40 training images. Increasing the size of the training dataset is expected to significantly improve the model's performance, providing more accurate and reliable predictions. This enhancement will be essential to achieve better segmentation results and ultimately more precise quantification of tissue ingrowth.

ACKNOWLEDGMENTS

This research was supported by the National Institutes of Health (NIH) grant R01 NS110710 (Principal Investigator: Brian Hoh) titled “Inflammatory Mediators and Mechanisms of Cerebral Aneurysm Formation and Rupture.” We also acknowledge the Human BioMolecular Atlas Program (HuBMAP) Undergraduate Student Internship Program for providing research support and the opportunity to contribute to computational microscopy and imaging studies. The authors express their gratitude for this funding, which made this work possible.

REFERENCES

- [1] Wardlaw, J. and White, P., “The detection and management of unruptured intracranial aneurysms,” *Brain* **123**(2), 205–221 (2000).
- [2] “Cerebral Aneurysms — ninds.nih.gov.” [https://www.ninds.nih.gov/health-information/disorders/cerebral-aneurysms#:~:text=A%20cerebral%20aneurysm%20\(also%20known,tissue%20\(called%20a%20hemorrhage\).](https://www.ninds.nih.gov/health-information/disorders/cerebral-aneurysms#:~:text=A%20cerebral%20aneurysm%20(also%20known,tissue%20(called%20a%20hemorrhage).) [Accessed 01-08-2024].
- [3] Andaluz, N. and Zuccarello, M., “Recent trends in the treatment of cerebral aneurysms: analysis of a nationwide inpatient database,” *Journal of neurosurgery* **108**(6), 1163–1169 (2008).
- [4] “Statistics and Facts - Brain Aneurysm Foundation — bafound.org.” <https://www.bafound.org/statistics-and-facts/#:~:text=An%20estimated%206.8%20million%20people,aneurysm%20ruptures%20every%2018%20minutes.> [Accessed 01-08-2024].
- [5] “Brain aneurysm - Diagnosis and treatment - Mayo Clinic — mayoclinic.org.” <https://www.mayoclinic.org/diseases-conditions/brain-aneurysm/diagnosis-treatment/drc-20361595#:~:text=Surgical%20clipping%20is%20a%20procedure,stop%20blood%20flow%20into%20it.> [Accessed 01-08-2024].
- [6] Campi, A., Ramzi, N., Molyneux, A. J., Summers, P. E., Kerr, R. S., Sneade, M., Yarnold, J. A., Rischmiller, J., and Byrne, J. V., “Retreatment of ruptured cerebral aneurysms in patients randomized by coiling or clipping in the international subarachnoid aneurysm trial (isat),” *Stroke* **38**(5), 1538–1544 (2007).
- [7] Hoh, B. L., Hosaka, K., Downes, D. P., Nowicki, K. W., Fernandez, C. E., Batich, C. D., and Scott, E. W., “Monocyte chemoattractant protein-1 promotes inflammatory vascular repair of murine carotid aneurysms via a macrophage inflammatory protein-1 and macrophage inflammatory protein-2–dependent pathway,” *Circulation* **124**(20), 2243–2252 (2011).
- [8] Bavinzski, G., Talazoglu, V., Killer, M., Richling, B., Gruber, A., Gross, C. E., and Plenck, H., “Gross and microscopic histopathological findings in aneurysms of the human brain treated with Guglielmi detachable coils,” *Journal of neurosurgery* **91**(2), 284–293 (1999).
- [9] Kosaraju, S. C., Park, J., Lee, H., Yang, J., and Kang, M., “Deep learning-based framework for slide-based histopathological image analysis,” *Scientific Reports* **12** (11 2022).